



NH₃-assisted synthesis of microporous silicon oxycarbonitride ceramics from preceramic polymers: a combined N₂ and CO₂ adsorption and small angle X-ray scattering study

Journal:	<i>Journal of Materials Chemistry A</i>
Manuscript ID:	TA-ART-08-2014-004233.R1
Article Type:	Paper
Date Submitted by the Author:	16-Oct-2014
Complete List of Authors:	Schitco, Cristina; Technische Universität Darmstadt, Fachbereich Material- und Geowissenschaften Seifollahi Bazarjani, Mahdi; Technische Universität Darmstadt, Fachbereich Material- und Geowissenschaften; Carl von Ossietzky Universität Oldenburg, Institut für Chemie Riedel, Ralf; Technische Universität Darmstadt, Fachbereich Material- und Geowissenschaften Gurlo, Aleksander; Technische Universität Darmstadt, Fachbereich Material- und Geowissenschaften

ARTICLE

NH₃-assisted synthesis of microporous silicon oxycarbonitride ceramics from preceramic polymers: a combined N₂ and CO₂ adsorption and small angle X-ray scattering study

Cite this: DOI: 10.1039/x0xx00000x

Cristina Schitco,^{a*} Mahdi Seifollahi Bazarjani,^{a,b} Ralf Riedel,^a and Aleksander Gurlo^{a, c}Received 00th January 2012,
Accepted 00th January 2012

DOI: 10.1039/x0xx00000x

www.rsc.org/

^a Technische Universität Darmstadt, Fachbereich Material- und Geowissenschaften, Jovanka-Bontschits-Strasse.2, D-64287 Darmstadt, Germany, E-mail: *schitco@materials.tu-darmstadt.de^b current address: Carl von Ossietzky Universität Oldenburg, Institut für Chemie, Carl von Ossietzky Strasse 9-11, D-26129 Oldenburg, Germany^c current address: Technische Universität Berlin, Fakultät III Prozesswissenschaften, Institut für Werkstoffwissenschaften und Technologien, Fachgebiet Keramische Werkstoffe, Hardenbergstraße 40, 10623 Berlin, Germany

We have developed a simple and general synthesis strategy to tune the chemical composition and pore size as well as the surface area of microporous ceramics. This method is based on modifying the structure of preceramic polymers through chemical reactions with NH₃ at 300-800 °C, followed by a thermolysis under an Ar atmosphere at 750 °C. Under these synthesis conditions a polysiloxane (SPR-212a, Starfire® Systems) and a polysilazane (HTT-1800, KiON Specialty Polymers) transform to microporous ceramics, while materials derived from a polycarbosilane (SMP-10, Starfire® Systems) remain non-porous, as revealed by N₂ and CO₂ adsorption isotherms. Small angle X-ray scattering (SAXS) characterization indicates that samples prepared from the polycarbosilane possess latent pores (pore size < 0.35 nm) which are not accessible in the gas adsorption experiments. The microporous silicon oxycarbonitride (SiCNO) ceramics synthesized from the polysilazane and polysiloxane by above-mentioned route possess surface area and micropore volume of as high as 250-300 m² g⁻¹ and 0.16 cm³ g⁻¹, respectively, as determined by N₂ adsorption method. The analysis of CO₂ adsorption isotherms by the Dubinin-Astakhov equation confirms a narrow pore size distribution in the ceramics derived from the polysilazane. Our synthesis strategy provides tools to engineer the microstructure, that is the chemical structure and porosity, of microporous SiCNO ceramics for potential applications in the fields of catalysis, gas adsorption and gas separation.

1. Introduction

Micro- and mesoporous polymer-derived ceramic (PDC) and their nanocomposites are of great technological importance for many emerging applications including gas separation and catalysis.¹⁻¹¹ PDCs are especially suitable for applications involving harsh environmental conditions because of their high thermal and chemical stability.¹²⁻¹⁹

Micro- and mesoporous PDCs with variable pore geometry, microstructure and specific surface area have been synthesized by the thermolysis of preceramic polymers (so-called polymer thermolysis route).^{6, 20-23} The polymer-to-ceramic transformation occurs through several distinctive stages, such as the decomposition of organic groups, accompanied by the release of gaseous species (H₂ and CH₄ and other volatile compounds).^{2, 3} The evolution of these gaseous species “nucleates” an intrinsic microporosity in as-formed products.³

However, the above-mentioned transient microporosity collapses as the thermolysis temperature increases, this process is driven by the spontaneous trend towards reduced surface energy.^{2, 3} The collapse of microporous structure begins at temperatures higher than ~450 °C and micropores, which are needed for applications, such as gas separation, gas adsorption or catalysis, are almost entirely eliminated at above 600 °C.^{3, 24} Above 800 °C the viscous flow and ripening of micropores lead to a macroporous ceramic with a low surface area.³ For instance, the development of microporosity at the temperature range of 400-800 °C in the thermolysis products of polysiloxane (PSO) have been extensively reported by several groups.²⁵⁻³¹ The main problem is the fast decrease in the developed microporosity at 700-800 °C, leading to low surface area solids at 700-800 °C.^{29, 30} Therefore, the challenge is to preserve the microporosity, developed in the PDCs during the polymer-to-ceramic transformation, at least up to 750 °C for the aforementioned applications.³

The goal of the present work is to design a chemical synthesis route with upscaling potential that allows for obtaining microporous PDCs with tunable pore size and composition.

The beneficial effect of NH_3 on the development of microporosity during the thermolysis of preceramic polymers has been demonstrated in several recent works as described below.³²⁻³⁴

Dismuskes et al. have demonstrated several generalized strategies for the synthesis of microporous silicon carbonitride (SiCN) and silicon imidonitride ($\text{Si}_3\text{N}_{4-2x}(\text{NH})_{3x}$) ceramics and ceramics.³³ In this study, the microporosity of ceramics is reinforced and consequently stabilized by incorporated filler particles at high temperatures (600-900 °C).³³ In this regard, four synthesis approaches have been successfully applied; they involve the controlled thermolysis of filler-containing polysilazanes (PSZs) at 600-900 °C under either an inert gas flow or a reactive NH_3 atmosphere.³²⁻³⁴ The main results of these works can be summarized as follows:

(i) The thermolysis of mixtures of PSZs with micron-sized ceramic fillers, such as Si_3N_4 , SiC, and AlN, in an inert atmosphere or under an NH_3 flow leads to ceramic-ceramic composites.³³

(ii) The thermolysis of a nanoscaled, PSZ/metal colloid of noble or transition metals (e.g. Ni, prepared by the condensation of Ni vapors into PSZ solutions) forms cermet nanocomposites.³³ However, the load of Ni nanoparticles is limited to 4-5 wt % and the size distribution of nanoparticles is not clear. Recently, we have invented a method to *in situ* form well-dispersed Ni nanoparticles (~3 nm, tunable up to 10 wt %) in PSZs,^{3, 4} which after thermolysis leads to microporous nickel silicon oxycarbonitride nanocomposite.

(iii) The thermolysis of PSZ/organometallic compositions in an inert or NH_3 atmospheres leads to the cermet nanocomposites.

(iv) The fourth method is based on the chemical synthesis of silicon imidonitrides from PSZs by thermolysis in an NH_3 atmosphere, that eliminates the most of carbon in the derived-PDCs.³²⁻³⁴ This method is discussed in detail in the subsequent paragraphs.

The thermolysis of PSZs under an NH_3 atmosphere provides an effective method to completely transform organosilicon bonds, such as Si-H, Si- CH_3 and Si- $\text{CH}=\text{CH}_2$ to imidonitride bonds.³³ The formation of imidonitride bonds is because of the reactions between the Si-H, Si- CH_3 and Si- $\text{CH}=\text{CH}_2$ bonds with NH_3 molecules followed by the subsequent condensation at high temperatures. As the thermolysis temperature exceeds 700-800 °C, the imidonitride bonds transform into Si-N bonds releasing H_2 (dehydrocoupling reactions). Therefore, organosilazane structure changes to silicon imidonitride structure at ~300-600 °C, while at ~800 °C, dominantly silicon nitride entity appears.

By the method (iv), silicon imidonitride compositions, $\text{Si}_3\text{N}_{4-2x}(\text{NH})_{3x}$, with high surface areas (300-600 $\text{m}^2 \text{g}^{-1}$) are synthesized.³³ The tailoring of pore size and composition of silicon imidonitrides by changing the thermolysis conditions and the type of PSZs are important developments in the field of solid base catalysts.³²⁻³⁴

It is important to emphasize that pure polysilazanes which are thermolyzed under an inert atmosphere lose their transient microporosity at above 600 °C, and stable microporosity at 700-900 °C is achievable only if the initial polysilazane contain filler particles or has reacted with organometallic ingredients. This is because the fillers or *in situ* formed metallic (nano)particles reduce

the viscose flow of the transient microporosity in SiCNs at high temperatures. Another explanation is that elimination of porosity and shrinkage is reduced by the presence of the solid phase, i.e. fillers, which regularly show no volume change creating a difference in coefficient of thermal expansion (CTE) between particles and the polymer-derived ceramic matrix. This hinders the closure of micro- and mesopores, providing escaping channels for the gaseous thermolysis products, leaving behind a porous ceramic phase after the polymer-to-ceramic transformation.³⁵

Therefore, the thermolysis products formed by above-mentioned four routes (i, ii, iii) under an inert atmosphere are microporous "cermet" SiCN (nano)composites and they can reach to surface areas as high as 400 $\text{m}^2 \text{g}^{-1}$ and micropore volumes up to 0.16 $\text{cm}^3 \text{g}^{-1}$ at 650 °C.³⁶

Thermolysis products under a reactive NH_3 atmosphere are cermet silicon imidonitrides (nano)composites with surface area of as high as 600 $\text{m}^2 \text{g}^{-1}$ and micropore volume up to 0.24 $\text{cm}^3 \text{g}^{-1}$ at 700 °C.³⁶

The higher surface area and pore volume of the silicon imidonitrides, produced under a reactive NH_3 atmosphere compared to those of the SiCNs synthesized under an inert atmosphere, suggest that the structural units, responsible for the formation of micropores, originate from SiN_4 and NSi_3 environments and micropores are not located in the carbon phase.

The study performed in the current work is motivated by two reasons: (i) the above-mentioned hypothesis about the role of SiN_4 and NSi_3 environments infer that the thermolysis under an NH_3 atmosphere (ammonolysis) of preceramic polymers leads to the formation of open micropores reinforced by a rigid amorphous network of *in situ* formed Si-N bonds. The latter resists the viscose flow and ripening of micropores even after further thermolysis at a temperature as high as 750 °C under an Ar atmosphere. The role of ammonia in the formation and stabilization of micropores in PDCs is not well understood. Here, we investigate systematically the role of ammonia on the formation of microporosity in PDCs; (ii) comprehensive synthesis methods for the preparation of microporous SiCNO ceramics (with no fillers) from preceramic polymers have not been established so far.

Therefore, in the present work main classes of preceramic polymers, that are polycarbosilanes, polysiloxanes and polysilazanes, have been applied as starting materials for the synthesis of microporous PDCs by an NH_3 -assisted thermolysis route. The suitability of preceramic polymers is determined by the reactive groups, such as Si-H bonds, which transform into silicon imide and silicon nitride bonds through dehydrocoupling and transamination reactions with NH_3 at high temperatures, respectively.

Therefore, based on the aforementioned criterion, commercially available polycarbosilane (SMP-10), polysiloxane (SPR-212a), and polysilazane (HTT-1800) have been subjected to an intermediate thermolysis step under an NH_3 atmosphere (ammonolysis step) at temperatures between 300-800 °C with the subsequent thermolysis under an Ar atmosphere at 750 °C for 3 h.

The analysis of porosity is performed by the N_2 and CO_2 adsorption methods applying BET (Brunauer-Emmett-Teller) theory and D-A (Dubinin-Astakhov) equation on the adsorption isotherms. The role of the ammonolysis step on the formation of micropores is proved by comparing the porosity characteristics of the specimens that are prepared by combined thermolysis steps under an NH_3 and

Ar atmospheres to those synthesized by a single thermolysis step under an Ar atmosphere. Finally, complementary to gas adsorption, small angle X-ray scattering (SAXS) characterization is applied to evaluate the porosity of specimens.

2. Experimental section

2.1. Materials

Commercially available polycarbosilane SMP-10 (Stafire® Systems), polysiloxane SPR-212a (Stafire® Systems), and polysilazane HTT-1800 (KiON Specialty Polymers) were used as starting preceramic polymers. Thermolysis was carried out in a horizontal tube furnace.

All preceramic polymers were handled under an inert atmosphere using Schlenk techniques. The samples were placed in quartz

crucibles inside a quartz tube in which the thermolysis atmosphere can be varied between NH₃ and Ar atmospheres.

The ammonolyzed Pol^TNH samples (where Pol = SMP-10, SPR-212a, and HTT-1800 and T denotes the ammonolysis temperature) were produced by thermolysis under an NH₃ atmosphere at temperatures ranging from 300-800 °C for 1 h with a heating rate of 100 °C h⁻¹.

The Pol^TNHAr ceramics were subsequently synthesized from the ammonolyzed Pol^TNH samples under an Ar atmosphere at 750 °C for 3 h with a heating rate of 50 °C h⁻¹.

The PolAr samples were produced by direct thermolysis under an Ar atmosphere at 750 °C for 3 h with a heating rate of 50 °C h⁻¹.

The above-mentioned sample preparation is schematically described in Figure 1, indicating the labels used for each sample.

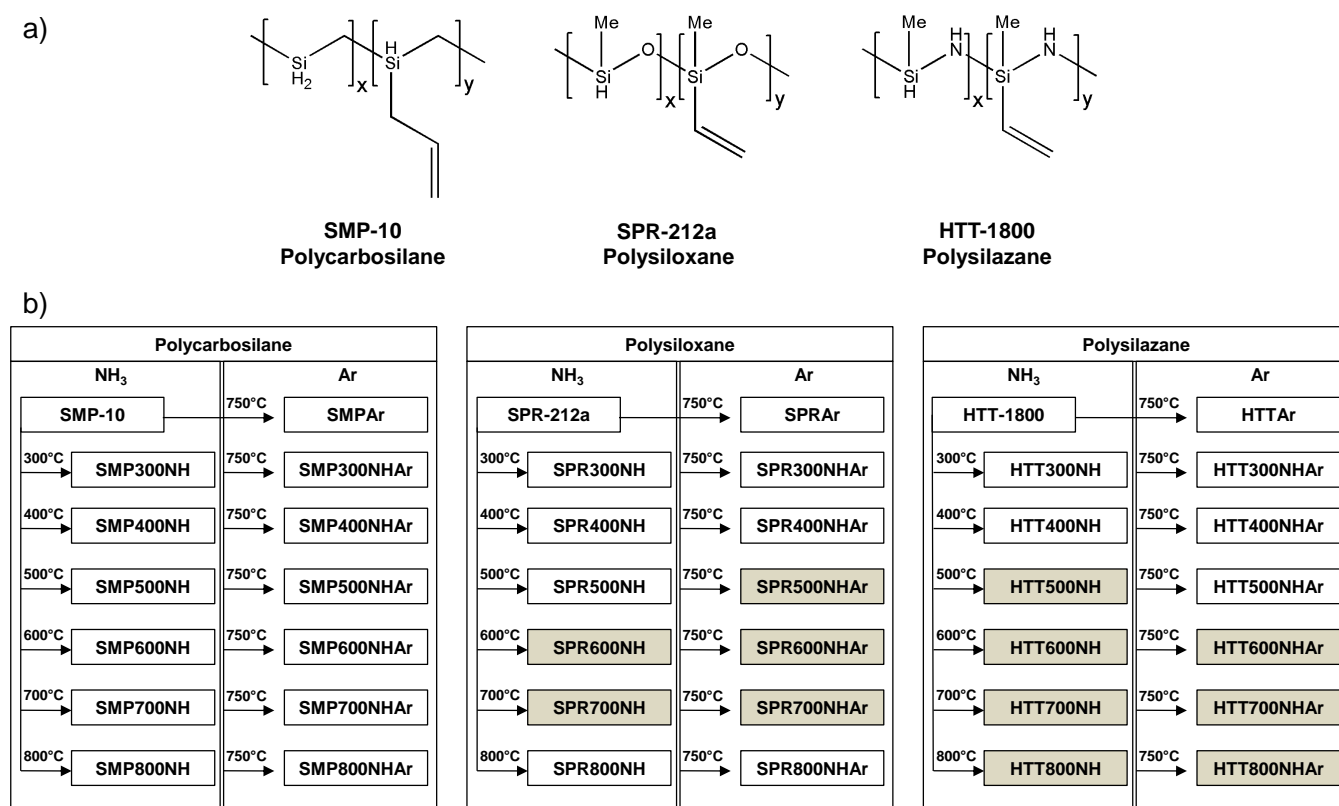


Figure 1. (a) Preceramic polymers in the current work. (b) Scheme of synthesis routes: a polycarbosilane (SMP-10), a polysiloxane (SPR-212a), and a polysilazane (HTT-1800) are thermolyzed under an NH₃ (at 300-800 °C for 1 h) and/or under an Ar atmospheres (at 750 °C for 3 h). Sample abbreviations “PolTNHAr” contain the polymer name (Pol), ammonolysis temperature (T) and the thermolysis atmospheres (NH₃ and/or Ar). Additionally, each polymer is thermolyzed at 750 °C under an Ar atmosphere, without ammonolysis step (PolAr samples) to compare with those prepared with an intermediate ammonolysis step (PolTNHAr samples). The microporous samples are highlighted in grey.

2.2. Characterization methods

2.2.1. Structural characterization and elemental analysis

X-ray diffraction was carried out using a STOE X-ray diffractometer (Germany) equipped with a Mo K_α radiation.

FTIR spectra were recorded on a Varian 670-IR (Agilent Technologies, USA) using 0.5-1 mg of powdered samples, pressed into KBr pellets.

The carbon content was determined in a carbon analyzer CS-800 (ELTRA GmbH, Germany), the nitrogen and oxygen content - in an N/O analyzer Leco TC-436 (Leco Corporation, USA). The hydrogen content was determined by the Mikroanalytisches Labor Pascher (Remagen, Bendorf-Germany) using the coupled plasma atomic

emission spectroscopy (Thermo Instruments, iCAP 6500) and elemental analyzer (Pascher). The silicon content was calculated by eq. (1).

$$\text{wt}\%(Si) = 100\% - \text{wt}\%(C) - \text{wt}\%(O) - \text{wt}\%(N) - \text{wt}\%(H) \quad (1)$$

2.2.2. Gas adsorption

N₂ adsorption was performed at -196 °C using an Autosorb -3B (Quantachrome Instruments, USA). The samples were preheated at 150 °C for 24 h under vacuum before the measurements. N₂ adsorption isotherms were recorded for all samples under investigation except those synthesized only under an NH₃ atmosphere at temperatures lower than 500 °C. The organic fragments in the latter materials are unstable during prolonged heating at 150 °C.

The N₂ isotherm at -196 °C was used to calculate the specific surface area $S_{N_2}^{BET}$ from the linear BET plots over the range $0.05 < p/p_o < 0.3$. The total pore volume $V_T^{N_2}$ was determined from the amount of vapour adsorbed at a relative pressure $p/p_o \approx 1$.³⁷ The micropore volume $V_{micro}^{t-N_2}$ was calculated using the de Boer's t-plot analysis.^{38, 39}

CO₂ adsorption analysis was performed at 0 °C by an ASAP-2000 automated volumetric analyzer (Micromeritics, USA) using the same outgassing procedure mentioned for N₂ adsorption. CO₂ adsorption isotherms were analyzed by the Dubinin-Astakhov (D-A) equation (eq. (2)).^{40, 41}:

$$V = V_o \exp \left[- \left(\frac{RT \ln \frac{p_o}{p}}{E} \right)^n \right] \quad (2)$$

where V denotes the amount of adsorbed gas per unit mass of adsorbent, V_o is the micropore volume (i.e. V_{micro}^{D-A, CO_2} in the present text), $RT \ln \frac{p_o}{p}$ is the adsorption potential. R , p and p_o refer to the gas constant; the equilibrium pressure and the saturation vapour pressure of adsorbate at a given temperature T , respectively.

E is the characteristic energy of adsorption (D-A energy) and n is the "heterogeneity factor".⁴²

The D-A equation is applied for the linearization of the adsorption data according to the following procedure.⁴¹ The y-intercept of $\left[\ln \left(\frac{p_o}{p} \right) \right]^n$ as a function of $\ln V$ yields the micropore volume (V_o) and the slope yields the D-A energy (E).

For experiments involving a single adsorbate, the D-A energy (E) could be expressed as $E = \beta E_o$, where β is the affinity coefficient that is characteristic of the adsorbate.⁴³ The affinity

coefficient β for CO₂ at 0 °C is equal to 0.35.⁴¹ E_o is the characteristic adsorption potential, related inversely to the pore size. For the characteristic adsorption potential (E_o) between 20 and 42 kJ mol⁻¹, the mean pore width (d_{D-A}) is estimated by the equation of Stoeckli et al. as follows:⁴⁴

$$d_{D-A}(nm) = \frac{10.8}{E/\beta - 11.4} \quad (3)$$

For E_o values lower than 20 kJ mol⁻¹ the Dubinin equation⁴⁵ is used:

$$d_{D-A}(nm) = \frac{24}{E/\beta} \quad (4)$$

2.2.3. Small angle X-ray scattering (SAXS)

SAXS experiments were performed at the Hamburger Synchrotronstrahlungslabor (HASYLAB) of the Deutsches Elektronen - Synchrotron (DESY) Research Centre of the Helmholtz Association, in Hamburg, Germany. The beamline A2 of the DORIS III storage ring was used, equipped with a two-dimensional MarMosaic CCD detector (Mar 225, Mar, Evanston, USA).

Powder samples were introduced in quartz capillaries (Hilgenberg GmbH, Germany) and the measurements were performed in transmission geometry.

The distance between sample to detector was 1.018 m, measuring scattering vector q in the range 0.2 to 3.5 nm⁻¹, (2θ (°) of 0.3 to 4.8). The scattering vector is expressed by eq. (5):

$$q = \frac{4\pi \sin \theta}{\lambda} \quad (5)$$

where θ is the scattering angle and λ is the X-ray wavelength ($\lambda = 1.5$ Å). Data are processed and converted into the diagrams of scattered intensities vs scattering vector (q) by the A2tool program. The intensity profile of an empty capillary is subtracted from those of the specimens.

The radius of gyration (R_g) and the Porod exponent (n) were determined in the Guinier and Porod regions, respectively.

The analysis of SAXS data is performed by the classical approach of Guinier,⁴⁶ which characterizes the pore size (or particle size) by one universal parameter, the radius of gyration (R_g).

R_g is the electronic radius of gyration of a particle about its electronic center of mass. In a porous system, the pore is considered as an electronic deficient void.³⁹ Therefore, R_g depends on both pore size and shape.⁴⁷ Accordingly, the scattering intensity for small q (corresponding to small 2θ values which fall typically in the SAXS range) is presented as follows:

$$I(q) = I(0) \exp \left[- \left(q R_g \right)^2 / 3 \right] \quad (6)$$

The Guinier approximation is valid for $qR_g < 1$. If the $I(q)$ curves are redrawn in the form of $\ln(I(q)) = f(q^2)$, R_g is determined from the slope of linear region. In case that none of the $\ln(I(q)) = f(q^2)$ relationships can be well fitted by the Guinier expression, then it is assumed that the system is consisted of pores with different radii of gyration. If it is assumed that the shapes of the pores are similar, then a pore size distribution for those pores can be simulated.

Therefore, based on $\ln(I(q)) = f(q^2)$ expressions using the experimental SAXS curves, an approximate pore-distribution function based on the radii of gyration in the Guinier coordinates and the approach of Kitaigorodskii is constructed.⁴⁸

The Kitaigorodskii approach has been used by Kyutt et al.⁴⁹ to study nanoporous carbon produced from polycrystalline carbide materials, and by Venhryn et al.⁵⁰ to investigate carbon-based materials, as well as by Gogotsi et al.⁵¹ to simulate nanoporous carbide-derived carbons.

In the Kitaigorodskii approach, it is assumed that the system under study contains a number of species with different size. Here, pores scatter distinctively based on the pore size. Therefore, the $I(q)$ curve is considered as a sum of $I_k(q)$ components corresponding to species k , which are formed by the pores of certain size.

In the next step, the linear region at the largest q of $\ln(I(q)) = f(q^2)$ plot is chosen and the tangent corresponding to this linear region of the $\ln(I(q)) = f(q^2)$ curve is drawn (Figure S1). The slope of the latter tangent yields the radius of gyration, R_{g1} , of the smallest pores, with a measurable scattering in the experiment ($R_{g1} = R_{g\min}$). The intercept of this latter tangent on the vertical axis, $I_1(0)$, gives the contribution of pores with the radius of gyration R_{g1} to the intensity of scattering, providing the possibility to determine their fraction. Afterwards, the $I_1(q)$, accounting for the pores with R_{g1} is subtracted from the experimental $I(q)$ curve. Then, redrawing the difference $I(q) - I_1(q)$ in the Guinier coordinates, and repeating the above-mentioned procedure, the contribution of the pores with the radius of gyration R_{g2} is estimated.

Later, the next difference ($I(q) - I_k(q)$) curve for the estimation of pores with R_{gk} is constructed. This procedure is continued successively until a linear region in the Guinier coordinates $\ln(I(q)) = f(q^2)$, close to $q=0$ is obtained.

The slope of the tangent drawn from the linear region of $\ln(I(q)) = f(q^2)$ (close to $q=0$) is related to the pores with the largest radius of gyration ($R_{g\max}$) which are detectable in the SAXS experiment. The extrapolation of this tangent to $q^2=0$ provides information about the relative number of these pores with $R_{g\max}$.

The volume fraction or mass fraction (assuming a uniform density) of pores with a given radius of gyration (R_{gk}) is estimated by:

$$m_k \propto I_k(0) / R_{gk}^3 \quad (7)$$

Finally, the average value of the radius of gyration R_g^{av} is calculated by:

$$R_g^{av} = \frac{\sum_k R_{gk} m_k}{\sum_k m_k} \quad (8)$$

3. Results and discussion

3.1. Structure and composition

The XRD characterization (Figure 2) reveals that all specimens studied in this work are amorphous. Table 1 summarizes the chemical composition of studied samples.

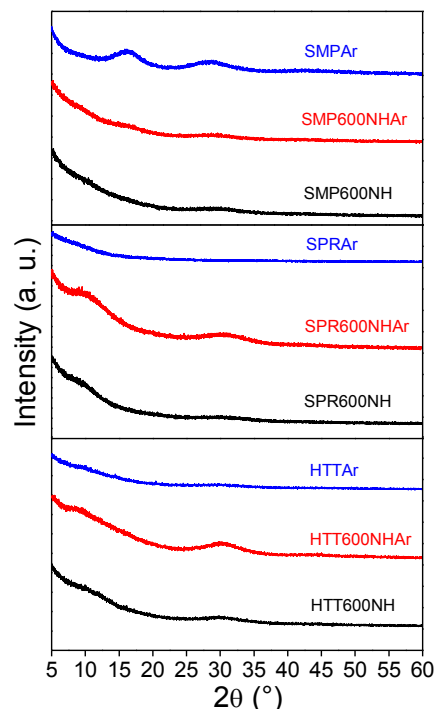


Figure 2. X-ray diffraction patterns of selected ceramers (SMP600NH, SPR600NH and HTT600NH) and ceramics (SMP600NHAr, SPR600NHAr, HTT600NHAr, SMPAr, SPRAr and HTTAr) derived from the polycarbosilane (a, SMP-10 samples), from the polysiloxane (b, SPR-212a samples), and from the polysilazane (c, HTT-1800 samples), after thermolysis step under an NH_3 atmosphere at 600 °C (black, SMP600NH, SPR600NH and HTT600NH), after thermolysis step under an NH_3 atmosphere at 600 °C followed by a thermolysis step under an Ar atmosphere at 750°C (red, SMP600NHAr, SPR600NHAr and HTT600NHAr), and after a single thermolysis step under an Ar atmosphere at 750°C (blue, SMPAr, SPRAr and HTTAr).

The results of the elemental analysis confirm that the NH_3 -assisted thermolysis of polycarbosilane, polysiloxane, and polysilazane leads to the nitrogen incorporation into the final ceramics. The SMP600NHAr and HTT600NHAr samples indicate 5.7 and 4.7 wt % more nitrogen compared to that of SMPAr and HTTAr samples (Table 1), respectively. This indicates that after the initial NH_3 -assisted thermolysis at 600 °C, the NH_3 reacts with silane groups (Si-H) partially forming Si-NH₂ substituents in the SMP600NH and HTT600NH samples. Further thermolysis of SMP600NH and HTT600NH at 750 °C under an Ar atmosphere involves transamination and dehydrocoupling reactions. The transamination between Si-NH₂ groups leads to the formation of Si-NH-Si and finally Si₃N environments with the loss of an NH_3 as by-product of the reactions. The loss of nitrogen molecules as a result of

transamination reactions in the second thermolysis step at 750 °C under an Ar atmosphere limits the nitrogen incorporation in the derived ceramics. However, as will be shown in section 3.2 and section 4, this could be sufficient to induce the formation of micropores.

The specimens after the ammonolysis step (i.e. Pol600NH) contain hydrogen, suggesting the formation of ceramers resembling both polymer and ceramic compositions. The subsequent heat-treatment under an Ar atmosphere at 750 °C of as-formed ceramers reduces the hydrogen content to the values comparable to those in the specimens synthesized by only a single thermolysis step under an Ar atmosphere (PolAr, Table 1).

Table 1. Chemical composition of SMP-10, SPR-212a, and HTT-1800-derived ceramics showing atomic and mass fractions of silicon, carbon, oxygen, nitrogen and hydrogen.

Sample	Atomic and mass (in parentheses) fraction %						Empirical formula
	Si	C	N	O	H		
SMP600NH	25.6 (59.3)	13.0 (13)	14.9 (17.3)	5.4 (7.0)	41.0 (3.4)		SiC _{0.51} N _{0.58} O _{0.21} H _{1.60}
SMP600NHAr	36 (60.2)	37.0 (26.7)	6.8 (5.7)	6.9 (6.6)	13.4 (0.8)		SiC _{1.03} N _{0.19} O _{0.19} H _{0.37}
SMPAr	35.8 (60.3)	47.3 (34)	0	5.2 (5.0)	11.7 (0.7)		SiC _{1.32} O _{0.15} H _{0.33}
SPR600NH	20.1 (54.5)	15.3 (17.8)	3.8 (5.2)	11.4 (17.7)	49.4 (4.8)		SiO _{0.57} C _{0.76} N _{0.19} H _{2.46}
SPR600NHAr	30.3 (54.0)	17.6 (13.4)	9.1 (8.1)	22.7 (23.2)	20.3 (1.3)		SiO _{0.75} C _{0.58} N _{0.30} H _{0.67}
SPRAr	33.6 (57.7)	31.9 (23.5)	0	18.1 (17.8)	16.4 (1.0)		SiO _{0.54} C _{0.95} H _{0.49}
HTT600NH	36.9 (68.7)	4.4 (3.6)	23.2 (21.5)	3.7 (4.1)	31.7 (2.1)		SiN _{0.63} C _{0.12} O _{0.10} H _{0.86}
HTT600NHAr	35.5 (60.1)	3.2 (2.3)	35.5 (30.4)	6.0 (5.8)	19.9 (1.2)		SiNC _{0.09} O _{0.17} H _{0.56}
HTTAr	33.1 (53.4)	22.5 (15.6)	31.8 (25.7)	5.6 (5.3)	6.9 (0.4)		SiN _{0.96} C _{0.68} O _{0.17} H _{0.21}

3.2. Porosity development and BET surface area as revealed by N₂ adsorption

Table 2 summarizes the BET surface areas ($S_{N_2}^{BET}$) and the types of isotherms for the specimens studied in this work. All samples, synthesized from the studied polycarbosilane indicate a type VI isotherm which is characteristic for stepwise multilayer adsorption on non-porous solids (Figure S2).³⁷ On the contrary, the specimens which are synthesised from polysiloxane and polysilazane develop a microporous structure under certain processing conditions, indicated by the Type I N₂ adsorption isotherms (Figure 3 a and b).

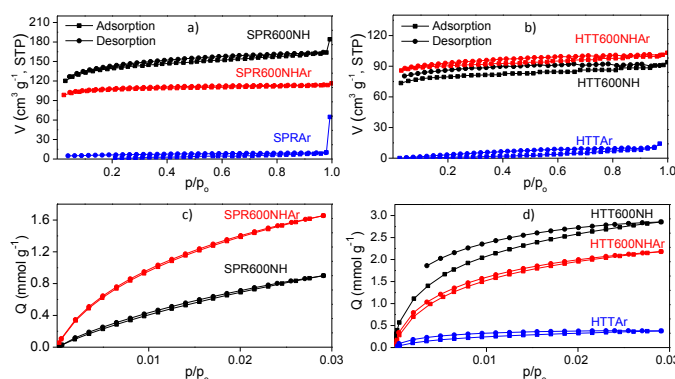


Figure 3. N₂ (a, b) and CO₂ (c, d) adsorption isotherms for representative ceramics, derived from polysiloxane (a, c, SPR-212a samples) and from polysilazane (b, d, HTT-1800 samples).

Thus, the results of the N₂ adsorption reveal that both polysilazane- and polysiloxane-derived materials form microporosity

during NH_3 -assisted thermosynthesis, while polycarbosilane-derived ceramics remain non-porous using the same procedure.

The polysiloxane-derived sample produced by a single thermolysis step under an Ar atmosphere (SPRAr) (without intermediate ammonolysis step) is a non-porous solid. The other polysiloxane-derived ceramics, namely SPR500NHAr, SPR600NHAr, and SPR700NHAr synthesized by the combination of intermediate ammonolysis step (thermolysis under an NH_3 atmosphere) and subsequent thermolysis under an Ar atmosphere develop a microporous structure during the ammonolysis step and the micropores do not collapse after further thermolysis under an Ar atmosphere at 750 °C (Table 2). In this regard, the SPR600NHAr ceramic shows the highest $S_{N_2}^{BET}$ of 306 m² g⁻¹ between all samples, synthesized from the polysiloxane by the NH_3 -assisted thermolysis route. Furthermore, polysiloxane-derived samples, synthesized under an NH_3 atmosphere at 600 °C show the highest $S_{N_2}^{BET}$ of 413 m² g⁻¹, which decreases to 77 m² g⁻¹ in the specimen prepared by a single ammonolysis step at 800 °C (Table 2). The formation of stable microporosity at about 750 °C by the above-mentioned NH_3 -assisted thermolysis route (using polysiloxanes with silane groups which react with NH_3 and with vinyl groups for crosslinking) is unique, and has not been reported so far, described as follows.

To the best of our knowledge, three micro- and mesoporous polysiloxane-derived ceramic systems (without sacrificial ingredients) have been reported.

(i) Literature survey shows that the micro- and mesoporous polysiloxane-derived ceramics with surface area, micropore volume and total pore volume of $547 \text{ m}^2 \text{ g}^{-1}$, $0.16 \text{ cm}^3 \text{ g}^{-1}$, and $0.30 \text{ cm}^3 \text{ g}^{-1}$, respectively, can be prepared after thermolysis at $600 \text{ }^\circ\text{C}$ under a N_2 atmosphere. However, the porosity is lost at $700\text{--}800 \text{ }^\circ\text{C}$. The addition of pre-thermolized polysiloxanes (as non-sacrificial fillers) to the same initial polysiloxane, followed by thermolysis (under the same processing conditions as that of the filler), reinforces the transient porosity and increases the mesoporosity of the polysiloxane-derived ceramer, e.g. surface area, micropore volume and total pore volume change to $561 \text{ m}^2 \text{ g}^{-1}$, $0.14 \text{ cm}^3 \text{ g}^{-1}$, and $0.48 \text{ cm}^3 \text{ g}^{-1}$, respectively.³⁰ For example, the incorporation of filler systems (carbon, pre-thermolized polysiloxane fillers) or by chemical modification of polysiloxane precursors, and their thermolysis under a N_2 atmosphere results in micro- and mesoporous ceramics with the surface area of $125 \text{ m}^2 \text{ g}^{-1}$ at temperatures as high as $1000 \text{ }^\circ\text{C}$.^{35, 52}

(ii) As shown recently, a vinyl-terminated polysiloxane (XP RV 200) thermolyzed at $800 \text{ }^\circ\text{C}$, forms stable microporosity with a high surface area and pore volume of $\sim 250 \text{ m}^2 \text{ g}^{-1}$ and $0.05 \text{ cm}^3 \text{ g}^{-1}$, respectively.^{25, 26} The above-mentioned microporosity could originate from the precipitation of free carbon phase at early stages of thermolysis, which reinforces the microporosity at temperature as high as $800 \text{ }^\circ\text{C}$. However, this system also loses its microporosity at higher temperatures. The stable porosity from this system enabled us to apply the SiOC ceramics incorporated with TiO_2 or ZnO nanoparticles for photocatalytic water decontamination.^{25, 26} In addition, the recent results indicate the selectivity of this microporous SiOC for gas separation.⁵

(iii) The sol-gel reaction of linear diethoxycarbosilane or dimethoxycarbosilane is the main route to high surface area ($\approx 745 \text{ m}^2 \text{ g}^{-1}$) amorphous microporous $[-\text{Si}(\text{O})\text{CH}_2-]_n$ hybrid polymer, while branched precursors (instead of linear) lead to the formation of micro- and mesoporous $[-\text{Si}(\text{O})\text{CH}_2-]_n$ hybrid polymer with even higher surface areas ($\approx 917 \text{ m}^2 \text{ g}^{-1}$).^{2, 53} The thermolysis of linear and branched $[-\text{Si}(\text{O})\text{CH}_2-]_n$ hybrid polymers at $1000 \text{ }^\circ\text{C}$ (no holding time) under an inert atmosphere leads to micro- and mesoporous SiOC ceramics with surface areas of 210 and $436 \text{ m}^2 \text{ g}^{-1}$, respectively. The thermolysis of linear $[-\text{Si}(\text{O})\text{CH}_2-]_n$ hybrid polymer at $1000 \text{ }^\circ\text{C}$ for 1 and 4 h, leads to significant reduction in the surface areas, 16 and $<10 \text{ m}^2 \text{ g}^{-1}$, respectively, while the surface areas of ceramics derived from branched $[-\text{Si}(\text{O})\text{CH}_2-]_n$ hybrid polymer are stable at $1000 \text{ }^\circ\text{C}$ after 1 and 4 h, 280 and $252 \text{ m}^2 \text{ g}^{-1}$, respectively.

The formation of stable microporosity in polysiloxane-derived samples by NH_3 -assisted thermolysis route developed here indicates the potential of this method for the preparation of microporous PDCs by other classes of preceramic polymers as well. Indeed, polysilazanes can be readily adapted by this technique and be transformed to microporous ceramics which is described below.

The $S_{\text{N}_2}^{\text{BET}}$ of polysilazane-derived samples reaches to the highest value of $400 \text{ m}^2 \text{ g}^{-1}$ in the specimen ammonolyzed at $500 \text{ }^\circ\text{C}$ and decreases to $231 \text{ m}^2 \text{ g}^{-1}$ as the ammonolysis temperature increases to $800 \text{ }^\circ\text{C}$ (Table 2). Dismukes et al. reported a similar finding, i.e. $S_{\text{N}_2}^{\text{BET}}$ as high as $200\text{--}400 \text{ m}^2 \text{ g}^{-1}$ and Type I adsorption isotherm for a polysilazane thermolyzed under an NH_3 atmosphere at $700\text{--}800 \text{ }^\circ\text{C}$.³³

Similar to the SPRAr sample, which is prepared by a single thermolysis step under an Ar atmosphere, the N_2 adsorption isotherm of HTTAr sample indicates a non-porous ceramic. On the other hand, the HTT600NHAr, HTT700NHAr, and HTT800NHAr samples retain their microporosity, developed during the ammonolysis step. The HTT600NHAr sample possesses the highest $S_{\text{N}_2}^{\text{BET}}$ of $266 \text{ m}^2 \text{ g}^{-1}$ between all samples, synthesized from the polysilazane by the NH_3 -assisted thermolysis route.

In summary, the results of the N_2 adsorption unambiguously underline the determining role of ammonolysis step on the formation of micropores. In this regard, both polysiloxane- and polysilazane-derived ceramics synthesised under NH_3 at $600 \text{ }^\circ\text{C}$ / Ar at $750 \text{ }^\circ\text{C}$ (SPR600NHAr and HTT600NHAr) indicate the largest surface area and micropore volume between all Pol^TNHAr ceramics.

The polycarbosilane-derived samples remain non-porous; this finding is in contrast to previous works that present the synthesis of a high surface area silicon carbide (SiC) with free carbon phase form polycarbosilane precursors (carbon-rich SiC).⁵⁴ In the latter case, the micropores exist in the carbon phase as they disappear after a thermolysis step under an air atmosphere, which leads to the removal of carbon. This finding confirms that the micropores (accessible by gas adsorption) in the above-mentioned SiC derived from a polycarbosilane polymer seem to be located in the free carbon phase. This is in agreement with our results, as the polycarbosilane-derived samples in the present work contain a low amount of free carbon, which consequently provides low gas adsorption sites.

However, we cannot exclude that the polycarbosilane-derived specimens studied here possess closed and /or latent micropores which could be inaccessible in gas adsorption experiments. The latter speculation is further confirmed by SAXS studies (section 3.5), indicating the presence of very small micropores inaccessible to N_2 and even CO_2 molecules in the gas adsorption techniques.

Table 2. BET surface areas ($S_{\text{N}_2}^{\text{BET}}$) and types of isotherms for the polycarbosilane, polysiloxane, and polysilazane-derived samples as revealed by N_2 adsorption.

Polycarbosilane			Polysiloxane			Polysilazane		
Sample	$S_{\text{N}_2}^{\text{BET}}$ ($\text{m}^2 \text{ g}^{-1}$)	Isotherm type	Sample	$S_{\text{N}_2}^{\text{BET}}$ ($\text{m}^2 \text{ g}^{-1}$)	Isotherm type	Sample	$S_{\text{N}_2}^{\text{BET}}$ ($\text{m}^2 \text{ g}^{-1}$)	Isotherm Type

SMP300NH	-	-	SPR300NH	-	-	HTT300NH	-	-
SMP400NH	-	-	SPR400NH	-	-	HTT400NH	-	-
SMP500NH	95	VI	SPR500NH	23	VI	HTT500NH	400	I
SMP600NH	66	VI	SPR600NH	413	I	HTT600NH	230	I
SMP700NH	48	VI	SPR700NH	160	I	HTT700NH	227	I
SMP800NH	9	VI	SPR800NH	77	VI	HTT800NH	231	I
SMP300NHAr	<6	VI	SPR300NHAr	86	VI	HTT300NHAr	<6	VI
SMP400NHAr	<6	VI	SPR400NHAr	70	VI	HTT400NHAr	<6	VI
SMP500NHAr	<6	VI	SPR500NHAr	300	I	HTT500NHAr	<6	VI
SMP600NHAr	16	VI	SPR600NHAr	306	I	HTT600NHAr	266	I
SMP700NHAr	8	VI	SPR700NHAr	195	I	HTT700NHAr	240	I
SMP800NHAr	34	VI	SPR800NHAr	64	VI	HTT800NHAr	189	I
SMPAr	14	VI	SPRAr	13	N/A	HTTAr	17	VI

3.3. The homogeneity and size of the pores

The analysis of the CO₂ adsorption isotherms provides additional information about the microstructure of specimens. The kinetic diameter of CO₂ (0.33 nm) is similar to that of N₂ (0.36 nm),⁵⁵ but the higher measurement temperature (0 °C) of the CO₂ adsorption isotherms results in the higher kinetic energies of CO₂ molecules. Therefore, CO₂ molecules at 0 °C are able to enter so-called ultramicropores (pore size < 0.7 nm),⁴³ that are hardly accessible to N₂ molecules.^{43, 56} In addition, CO₂ adsorption isotherms, measured up to 1 atm are not sensitive to pores larger than 1 nm.⁵⁷

In contrast, the N₂ adsorption isotherms, measured at -196 °C accounts for the presence of supermicropores which are between 0.7-2 nm.^{43, 57} The modelling of CO₂ adsorption isotherms is performed by Dubinin-Astakhov equation (eq. (2)) as described in the experimental section, allowing the D-A exponent to vary (Figure 4).

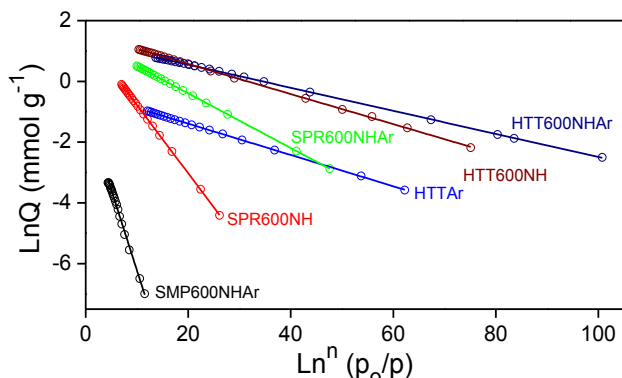


Figure 4. Dubinin-Astakhov (D-A) plots calculated from the CO₂ adsorption isotherms.

The D-A exponents (n), D-A energies (E), and the mean pore widths (d_{D-A}), are calculated from the D-A plots and are listed in Table 3.

The D-A exponent (n in eq.(2)) is referred to “heterogeneity factor”,⁴² that is related to the heterogeneity of the pore size distribution. It has been found that activated carbons with a rather broad pore size distributions possess a value of $n \approx 1$,^{41, 58} while $n \approx 2$ is characteristic for a material with a homogeneous distribution of micropores,^{58, 59} and a value of $n \geq 3$ is distinctive for zeolites, and molecular sieve carbons.⁶⁰

Figure 5 displays the total pore volume $V_T^{N_2}$ and the micropore volume $V_{micro}^{t-N_2}$ of the SPR600NH, SPR600NHAr, HTT600NH, and HTT600NHAr samples, calculated from the N₂ adsorption

isotherms. $V_T^{N_2}$ and $V_{micro}^{t-N_2}$ are compared with the micropore volume V_{micro}^{D-A,CO_2} , estimated from the CO₂ adsorption isotherms.

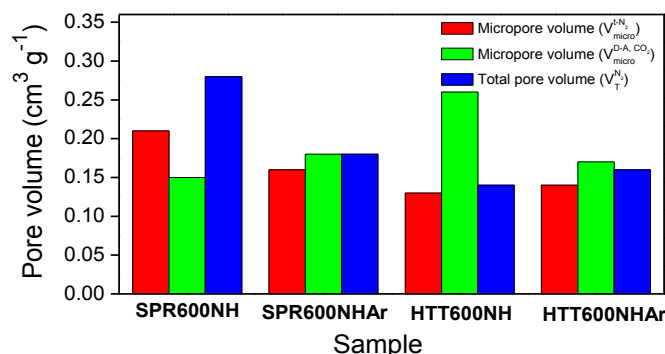


Figure 5. Micropore volume calculated from N₂ and CO₂ adsorption, $V_{micro}^{t-N_2}$ and V_{micro}^{D-A,CO_2} , respectively, as well as total pore volume from N₂ adsorption, $V_T^{N_2}$, for SPR600NH, SPR600NHAr, HTT600NH, and HTT600NHAr samples.

The SPR600NH sample indicates the $V_{micro}^{t-N_2}$ and $V_T^{N_2}$ of 0.21 cm³ g⁻¹ and 0.28 cm³ g⁻¹, respectively, implying a significant amount of mesopores in SPR600NH. In addition, as V_{micro}^{D-A,CO_2} (0.15 cm³ g⁻¹) is significantly less than $V_{micro}^{t-N_2}$ (0.21 cm³ g⁻¹), this specimen possesses supermicropores (micropores larger than 0.7 nm) that are not filled with CO₂ up to the measurement pressure of 1 atm.

In the SPR600NHAr sample, prepared by the thermolysis of SPR600NH under an Ar atmosphere, $V_{micro}^{t-N_2}$ and $V_T^{N_2}$ decrease to 0.16 and 0.18 cm³ g⁻¹, respectively, compared to those of SPR600NH, 0.21 and 0.28 cm³ g⁻¹, respectively. But, the fraction of micropores (taken as the ratio of $V_{micro}^{t-N_2}$ to $V_T^{N_2}$), increases from 0.75 to 0.89, in SPR600NH to SPR600NHAr samples, respectively.

Thus, during the thermolysis under an Ar atmosphere, further ceramization of the samples and the elimination of larger pores occur concomitantly (Figure 5, Table 3). As V_{micro}^{D-A,CO_2} (0.18 cm³ g⁻¹) is comparable to $V_{micro}^{t-N_2}$ (0.16 cm³ g⁻¹) for SPR600NHAr sample, this sample possesses a significant amount of supermicropores that are accessible to both N₂ and CO₂ molecules, which would correspond to the pore size range of 0.7-1 nm.⁵⁷

The D-A exponent, D-A energy, and mean pore size width d_{D-A} (Table 3) provide further evidence about a narrower distribution of micropores in SPR600NHAr sample if compared to those of SPR600NH specimen. The D-A exponent (1.82) and the D-A energy (8.5 kJ mol⁻¹) of the SPR600NHAr sample are larger than those found for SPR600NH specimen, i.e. 1.54 and 6 kJ mol⁻¹, respectively, indicating smaller mean micropore size (d_{D-A}) in SPR600NHAr sample if compared to that of SPR600NH sample, i.e. 0.8 nm and 1.4 nm, eq. (3) and eq. (4), respectively.

The HTT600NH specimen exhibits $V_{micro}^{t-N_2}$ and $V_T^{N_2}$ of 0.13 and 0.14 cm³ g⁻¹, respectively, which are significantly lower than those of SPR600NH material, 0.21 and 0.28 cm³ g⁻¹, respectively. However, the fraction of micropores taken as the ratio of $V_{micro}^{t-N_2}$ to $V_T^{N_2}$ is larger in HTT600NH (0.93), if compared to that of SPR600NH (0.75).

The HTT600NH sample has the highest value of V_{micro}^{D-A,CO_2} (0.26 cm³ g⁻¹) among all samples for which the CO₂ adsorption isotherms are recorded. The V_{micro}^{D-A,CO_2} (0.26 cm³ g⁻¹) is two times larger than the $V_{micro}^{t-N_2}$ (0.13 cm³ g⁻¹) indicating significant ultramicroporosity (pore size < 0.7 nm) in the HTT600NH specimen. The HTT600NHAr sample, derived from the latter by the treatment in an Ar atmosphere, loses some of its ultramicroporosity; as the V_{micro}^{D-A,CO_2} in this material decreases to 0.17 cm³ g⁻¹ which is comparable to $V_{micro}^{t-N_2}$ and $V_T^{N_2}$.

Similar to the SPR600NHAr material, HTT600NHAr sample consists mostly of supermicropores in the range of 0.7-1 nm that is accessible to both N₂ and CO₂ molecules.

The HTT600NHAr material is characterized by a narrow pore size distribution of micropores, revealed by the D-A exponent and D-A energy of 2.07 and 11 kJ mol⁻¹, respectively. As the D-A exponent of HTT600NH sample (i.e. 1.85) is smaller than that of the HTT600NHAr specimen (i.e. 2.07), the size distribution of the former material is less heterogeneous although the mean pore width could be similar, i.e. 0.5 nm for both HTT600NH and HTT600NHAr, respectively (eq. (3)).

The HTTAr sample has a micropore volume V_{micro}^{D-A,CO_2} of only 0.03 cm³ g⁻¹, however the larger values for the D-A exponent and D-A energy, 1.97 and 10.2 kJ mol⁻¹, respectively, (Table 3) indicate a narrow distribution of micropores and a small mean micropore width (i.e. 0.6 nm, eq. (3)).

For polycarbosilane-derived materials, the CO₂ adsorption isotherm is recorded only for the SMP600NHAr sample. As displayed in the Table 3, the SMP600NHAr sample has low amount of micropores associated to only 0.03 cm³ g⁻¹ of micropore volume V_{micro}^{D-A,CO_2} , with a broad pore size distribution as indicated by the small D-A exponent of 1.17. The D-A energy is small (3.9 kJ mol⁻¹), corresponding to a large micropore width of 2.2 nm (eq. (4)).

In summary, the Dubinin-Astakhov analysis of CO₂ adsorption isotherms provides important information on the homogeneity and size of the micropores. Polysilazane-derived ceramics indicate the highest degree of homogeneity and the smallest mean pore size. In contrast, the polysiloxane-derived samples show larger average micropore size with higher degree of heterogeneity in the micropores. HTT600NH sample has the highest V_{micro}^{D-A,CO_2} among all samples which could be because of the highest ultramicroporosity in its microstructure.

Table 3. $S_{CO_2}^{BET}$ and $S_{CO_2}^{D-A}$ surface areas, D-A exponent, characteristic energy (D-A energy), and mean pore size (d_{D-A}) as calculated from the CO₂ adsorption isotherms; the radii of gyration (R_g^{av}) and Porod exponent (n) as determined from the SAXS experiments, and $V_{micro}^{t-N_2}$ and $V_T^{N_2}$ as calculated from N₂ adsorption isotherms are provided.

Sample	$S_{CO_2}^{BET}$ (m ² g ⁻¹)	$S_{CO_2}^{D-A}$ (m ² g ⁻¹)	$V_{micro}^{t-N_2}$ (cm ³ g ⁻¹)	V_{micro}^{D-A,CO_2} (cm ³ g ⁻¹)	$V_T^{N_2}$ (cm ³ g ⁻¹)	D-A exponent	D-A energy (kJ mol ⁻¹)	d_{D-A} (nm)	R_g^{av} (nm)	n
SMP600NH	-	-	-	-	-	-	-	-	0.12	3.5
SMP600NHAr	6	50	0	0.03	0.02	1.17	3.9	2.2	no Guinier range	3.3
SMPAr	-	-	-	-	-	-	-	-	no Guinier range	3.7
SPR600NH	240	310	0.21	0.15	0.28	1.54	6.0	1.4	no Guinier range	3.6
SPR600NHAr	270	416	0.16	0.18	0.18	1.82	8.5	0.8	no Guinier range	3.7
SPRAr	-	-	-	-	-	-	-	-	no Guinier range	3.8
HTT600NH	357	641	0.13	0.26	0.14	1.85	11.5	0.5	0.20	3.5
HTT600NHAr	279	426	0.14	0.17	0.16	2.07	11.0	0.5	0.20	3.4
HTTAr	57	68	0	0.03	0.02	1.97	10.2	0.6	0.50	3.5

3.4. Nature of adsorbing surfaces

The Dubinin-Astakhov analysis of CO₂ adsorption isotherms indicates unambiguously that all specimens, for which CO₂ adsorption isotherms are recorded, possess higher surface areas calculated by the D-A method ($S_{CO_2}^{D-A}$) than those calculated by the BET method ($S_{CO_2}^{BET}$) (Figure 6 b). The reason for the difference

between $S_{CO_2}^{D-A}$ and $S_{CO_2}^{BET}$ could be because of the different assumptions applied for the D-A and BET theories. For instance, the adsorption mechanism in the D-A theory is based on the micropore filling mechanism, while in the BET theory a multilayer adsorption is assumed.

In addition, $S_{CO_2}^{BET}$ from the analysis of the CO_2 adsorption isotherms at $0^\circ C$ is compared with $S_{N_2}^{BET}$ from the analysis of the N_2 adsorption isotherms at $-196^\circ C$ (Figure 6 b, Table 2 and 3).

The comparison of $S_{CO_2}^{BET}$ and $S_{N_2}^{BET}$ allows us to distinguish between two cases (Table 2 and Table 3):

- (i) $S_{CO_2}^{BET} > S_{N_2}^{BET}$ found for polysilazane-derived materials, i.e. HTT600NH, HTT600NHAr and HTTA_r, and
- (ii) $S_{CO_2}^{BET} < S_{N_2}^{BET}$ found for polysiloxane-derived materials, i.e. SMP600NHAr, SPR600NH, and SPR600NHAr.

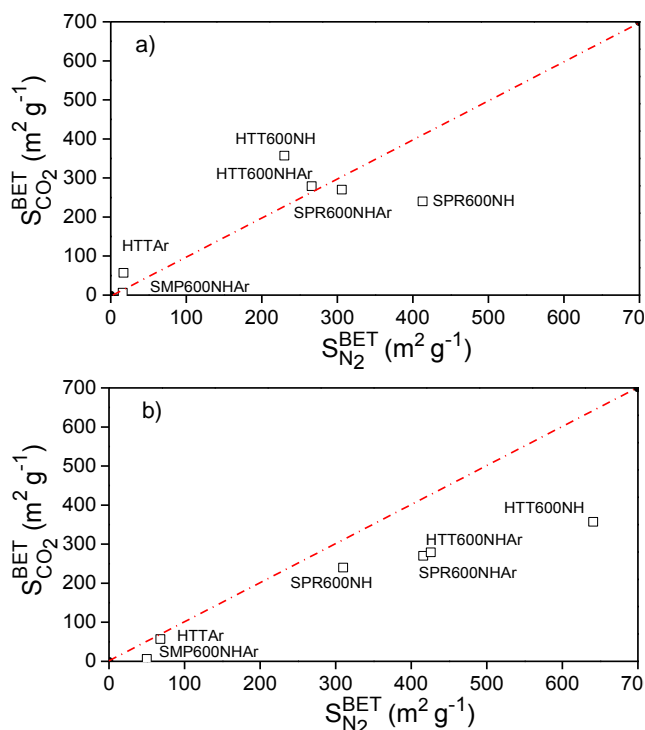


Figure 6. (a) Relationship between $S_{N_2}^{BET}$ and $S_{CO_2}^{BET}$ surface areas calculated from the N_2 and CO_2 adsorption isotherms. (b) Relationship between $S_{CO_2}^{D-A}$ and $S_{CO_2}^{BET}$ surface areas calculated from the CO_2 adsorption isotherms (See text for details).

Further analysis of the Table 2 and Table 3 indicates that the largest difference (more than $100 m^2 g^{-1}$) between BET surface area calculated from the CO_2 and N_2 adsorption isotherms, that is $\Delta S_{CO_2-N_2}^{BET} = S_{CO_2}^{BET} - S_{N_2}^{BET}$, is observed for samples that are synthesized under ammonia at $600^\circ C$ (Figure 6 a, SPR600NH and HTT600NH), while $\Delta S_{CO_2-N_2}^{BET}$ is less than $50 m^2 g^{-1}$ for all samples that are made by the thermolysis step under an Ar atmosphere at $750^\circ C$ (Table 3, HTTA_r, SMP600NHAr, SPR600NHAr and HTT600NHAr).

The aforementioned difference between $S_{CO_2}^{BET}$ and $S_{N_2}^{BET}$ can be ascribed to the difference in the composition of the specimens synthesized from polysilazane and polysiloxane, which in turn leads to the variation in the polarity and nature of pore surfaces.

We consider two effects, i.e. (i) the specific interaction of CO_2 with basic surface sites, and (ii) the polarization of N_2 molecules in the vicinity of polar hydroxylated surfaces.⁶¹ It is known that the $S_{N_2}^{BET}$ of hydroxylated polar surfaces is overestimated because of the specific interaction of N_2 with polar surfaces that leads to smaller cross-sectional area of N_2 , if compared to the standard value, 0.135 vs. $0.165 nm^2$, respectively.⁶¹

The specific interaction of CO_2 with basic imide groups results in higher apparent surface area calculated from the CO_2 adsorption isotherms.⁶²

The polysilazane-derived specimens, synthesized under an NH_3 atmosphere at $600^\circ C$, with high hydrogen and nitrogen content (Table 1), possess imidonitride ($Si_3N_{4-2x}(NH)_{3x}$) fragments. As shown in Figure S3, the IR spectra of these specimens displays bands at $3387 cm^{-1}$ and $1185 cm^{-1}$ which correspond to N-H stretching and deformation vibrations in the Si-NH-Si bonds, respectively. The dominant bands around $1000-900 cm^{-1}$ are attributed to Si_2N vibrations.

The imide groups adsorb preferentially CO_2 that in turn is found as the higher apparent CO_2 adsorption and higher $S_{CO_2}^{BET}$. The IR spectra of polysiloxane-derived specimens with high hydrogen and oxygen content (Table 1) display weak bands at $3450 cm^{-1}$ and $960 cm^{-1}$ (Figure S3) that are characteristic for Si-OH bonds, the latter polarize N_2 molecules leading to the higher $S_{N_2}^{BET}$.

These effects are more pronounced in the specimens subjected to an ammonolysis step only, i.e. in HTT600NH and SPR600NH materials due to the presence of above-mentioned specific interactions.

3.5. Porosity characterization as revealed by small-angle X-ray scattering

In this section, the size of pores obtained from the modelling of the small-angle X-ray scattering (SAXS) results is compared to those obtained from the gas adsorption experiments. Figure 7 displays the log-log plots of the scattering curves for the specimens prepared based on different preceramic polymers, (a) the polycarbosilane (SMP-10), (b) the polysiloxane (SPR-212a), and (c) the polysilazane (HTT-1800).

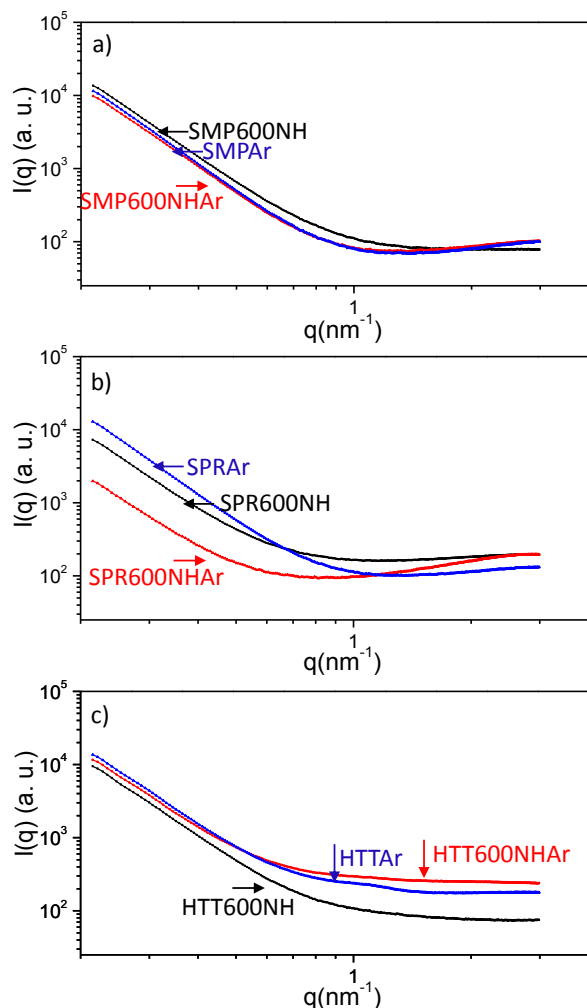


Figure 7. SAXS curves of specimens derived from polycarbosilane (a), polysiloxane (b), and polysilazane (c) precursors. For the sample notation, see Figure 1 b.

The scattering cross-section in log-log plot, should ideally consist of two steep lines nearly parallel to each other, separated by a plateau.⁶³ At low scattering vector (q), the scattering intensity corresponds to the scattering dominated by macropores and is proportional to q^{-4} . Therefore, the intensity should decrease linearly with a slope of -4 in a log-log plot. Then, as the plateau regime is approached, the micropore contribution appears to govern the scattering.

Finally, another linear decrease (a second steep line) is reached when $qR_g \gg \sqrt{6}$. The latter regime is not measured in our samples, because the scattering was recorded until $q=3 \text{ nm}^{-1}$. In addition, in the case of such samples as SPR600NH, SPR600NHAr, SPRAr, SMP600NHAr and SMPAr, the scattering intensity is significantly affected by Bragg reflections (Figure 7 and Figure S4 and S5 in SI).

The shape of the scattering curves of the specimens in the current work depends mainly on the type of initial preceramic polymer used for the synthesis of ceramers and ceramics. Therefore, using the classification of Kalliat et al.⁶⁴, our specimens can be classified into three types of profiles:

Type 1: the profile of scattering curves of SMP600NH, HTT600NH and HTT600NHAr samples, at low q the scattering intensity is nearly proportional to q^{-4} , while at high q the scattering intensity is almost constant (Figure S5 a). This profile suggests two types of inhomogeneities with different average dimensions, that are macropores and micropores. The scattering of the former (i.e. “macropores, large inhomogeneities”) decreases rapidly as q increases, while the scattering of the latter (i.e. “micropores, small inhomogeneities”) produces a relatively weak but constant scattering at high q . This profile of scattering corresponds nearly to the ideal scattering cross section as mentioned already.

Type 2: the profile of scattering curves of SPR600NH, SPR600NHAr, SPRAr, SMP600NHAr and SMPAr sample, at low q , is nearly proportional to q^{-4} , while at high q ($q > 1 \text{ nm}^{-1}$) the scattering intensity increases and a rather broad peak at even higher q is found (Figure S5 b). Similar peak at $q \approx 3 \text{ nm}^{-1}$, corresponding to a Bragg spacing of 2 nm (20 Å), is reported by Hirsch et al.⁶⁵ in coals and is assigned to the scattering centres, consisted of a few layers of planar aggregates with aromatic rings and is found by Kalliat et al.⁶⁴ in coal samples as well. Here, this peak is observed only in materials with high carbon content (Table 1); and it could originate from carbon-rich domains. Due to this peak, the scattering from the micropores in these samples cannot be assessed, albeit the microporosity of these specimens is confirmed by the N_2 and CO_2 adsorption isotherms. The macropore structures in SPR600NH, SPR600NHAr, SPRAr, SMP600NHAr and SMPAr ceramics is similar to those found in Type 1 (SMP600NH, HTT600NH and HTT600NHAr materials).

Type 3: the start of profile of the scattering curve of the HTTAr specimen is similar to the Type 1 and 2 materials. In other words, the scattering intensity at low q is nearly proportional to q^{-4} , indicating similar macropore structure as the Type 1 and 2 specimens (Figure S5 c). At higher q ($q > 1 \text{ nm}^{-1}$) a weak outer portion (Figure S5 c) of the scattering curve is found, and then the scattering intensity remains nearly constant. This outer portion of the scattering curve could be attributed to three contributions, (a) the tail of the inverse-fourth-power scattering from the macropores, (b) the scattering of carbon-rich domains (taking into account a rather high carbon content in this specimen, see Table 1), and (c) the scattering of large micropores.

Figure 8 displays the scattering curves of HTT600NHAr, SMP600NH, HTT600NH, and HTTAr materials in the Guinier coordinates, $\ln(I(q)) = f(q^2)$. Only these specimens display the Guinier range and other materials possess a maximum at $q > 1 \text{ nm}^{-1}$ and do not fall under the Guinier formalism. Therefore, R_g is determined only for the specimens for which a linear range in the Guinier coordinates is found. The calculated Porod exponent (n) for all samples is in the range of 3-4. This range is characteristic for the scattering of the external surfaces of the powder grains and/or macropores.

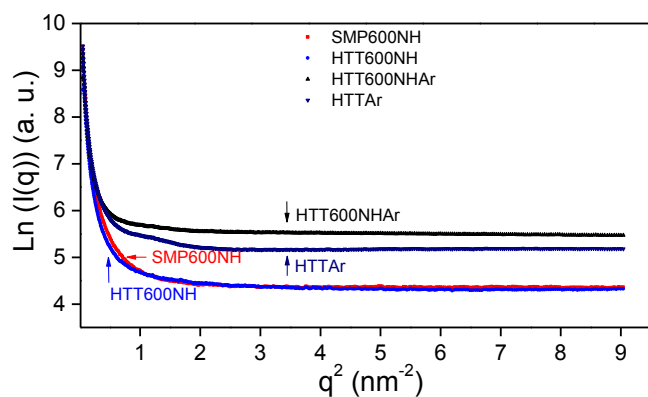


Figure 8. SAXS curves in the Guinier coordinates of SMP600NH, HTT600NH, HTT600NHAr, and HTTA specimens.

As displayed in Table 3, both HTT600NH and HTT600NHAr material possess the R_g^{av} of 0.2 nm, and the HTTA sample has the highest R_g^{av} value of 0.5 nm. The pore size (d_{D-A}) derived from the D-A analysis of the CO₂ adsorption isotherms follows the same trend, that is d_{D-A} = 0.5 nm for the HTT600NH and HTT600NHAr samples, and the HTTA specimen possesses a slightly higher d_{D-A} of 0.6 nm. Almost a monodisperse Guinier behavior ($\ln(I) \sim -q^2 R_g^2 / 3$) over a broad range of q^2 is found particularly for HTT600NHAr sample (Figure 8 and Figure S1), which agrees well with the homogeneous pore size distribution (D-A exponent of 2.07) derived from D-A analysis. The D-A analysis of the CO₂ gas adsorption isotherms and the SAXS results confirm that the HTT600NHAr and HTT600NH ceramics contain a significant amount of small micropores and narrow pore size distributions.

The SMP600NH sample is the only polycarbosilane-derived ceramic for which the Guinier range is found. This material displays a very small R_g^{av} of about 0.12 nm. Hypothetically, other polycarbosilane-derived samples possess latent pores which are not accessible in the gas adsorption experiments. The latent porosity refers to the open pores smaller than the size of probe molecules (CO₂ and N₂) used in the gas adsorption. Hence, the latent porosity is associated with ultramicropores with the pore size < 0.35 nm.³⁹ Such micropores could play a major role in the membranes used for hydrogen separation where an effective pore size of about 0.3 nm is required.^{9, 66-69}

4. Origin of microporosity in polymer-derived ceramics

The origin of transient microporosity in PDCs has been an elusive question which has not been comprehensively addressed so far. It is generally believed that during polymer-to-ceramic transformation a transient microporosity develops which is unstable and diminishes as the thermolysis temperature increases.

The formation of above-mentioned transient microporosity is usually accompanied by the release of small gaseous species, such as CH₄, NH₃ and H₂. Therefore, the nucleation and growth of microporosity could be assigned to the formation and release of small gaseous species. However, literature survey indicates that there are classes of microporous PDCs that the microporosity already exists in the microporous units of initial preceramic

polymer. For example, the thermolysis of micro- and mesoporous (hybrid) organosilicon polymers at $T < 1100$ °C results in the formation of micro- and mesoporous silicon-based ceramics. Depending on the structure of the initial organosilicon polymers, different micro- and mesoporous oxide and non-oxide ceramics in SiOC^{53, 70} and Si₃N_{4-2x}(NH)_{3x}^{36, 71-77} families have been synthesized.²

In other words, the formation of gaseous species during polymer-to-ceramic transformation as a result of such reactions as transamination, condensation, and dehydrocoupling leads to microporous units that are actually responsible for the microporosity of subsequent ceramic entity.

Therefore, micropore units could exist already in the initial structure of micro- and mesoporous (hybrid) organosilicon polymers² or be created during polymer-to-ceramic conversion of preceramic polymers by aforementioned reactions.

However, the micropore units are usually unstable (collapse and close) at temperatures as high as 700-800 °C. In order to understand the micropore units, we make an analogy with microporous silica as follows.

Microporous amorphous silica is made of 4-, 5-, 6-, 7-, and 8-membered silicon containing ring clusters made of siloxane (Si-O-Si) bonds (Figure 9 a).^{78, 79} However, the overall bonding strength of Si-O-Si bonds limits the microporosity of amorphous silica to well below 700 °C.

The partial or complete replacement of bivalent Si-O-Si (OSi₂) bonds with non-oxide bonds with higher bonding density, such as nitrogen and carbon provides more robust microporous units composed of trivalent Si-N-Si (NSi₃) and tetravalent Si-C-Si (CSi₄) bonds, Figure 9 b and c, respectively.

The 4-, 5-, 6-, 7-, and 8-membered silicon containing ring clusters composed of trivalent Si-N-Si and tetravalent Si-C-Si bonds are more robust than their Si-O-Si counterparts. However, this enhanced robust nature is at the expense of smaller micropore units which could make them inaccessible to the probe molecules or useless for the intended application e.g. gas separation or gas adsorption.

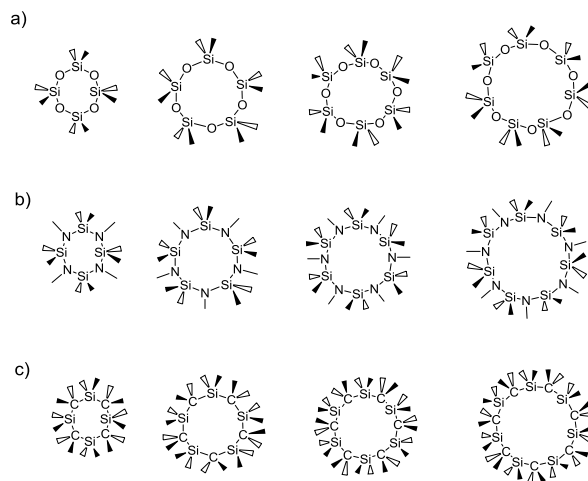


Figure 9. From left to right, 4-, 5-, 6- and 7- membered (8-membered is not shown) silicon containing ring clusters composed

of bivalent Si-O-Si (a), trivalent Si-N-Si (b), and tetravalent Si-C-Si bonds (c).

However, silicon oxycarbonitrides could have ideal ratios of more stable (but smaller) trivalent Si-N-Si, tetravalent Si-C-Si micropore clusters together with less stable (but larger) bivalent Si-O-Si micropore clusters, which survive the final thermolysis temperature. These ideal silicon oxycarbonitride compositions lead to stable micro- and mesoporous PDCs.

The synthetic strategy developed here targets the above-mentioned (potentially existing) ideal silicon oxycarbonitride compositions which are stable microporous ceramic solids with accessible and tailored micropores, which could be applicable for gas adsorption, gas separation or catalysis.

Extensive solid state NMR and pair distribution function (PDF) analysis is under investigation to find these ideal chemical compositions and their chemical environments in microporous and non-microporous PDCs which are developed in this study. These results are intensively under investigations in our studies to tailor stable microporous ceramics for a variety of important applications.

5. Conclusions

An NH₃-assisted thermolysis technique is successfully employed to synthesize microporous SiCNO ceramics from preceramic polymers. The results of the N₂ adsorption unambiguously confirm the determining role of ammonolysis step on the formation of micropores. It is found that both polysiloxane and polysilazane-derived materials ammonolysed at 600 °C (SPR600NHAr and HTT600NHAr, respectively) indicate the largest surface area and micropore volume between all samples in this work.

Combined N₂ and CO₂ adsorption isotherms as well as SAXS characterizations provide an overview of the homogeneity and size of the (micro)pores, as well as the nature of adsorption sites in the synthesized SiCNO ceramics.

The D-A analysis of CO₂ adsorption isotherms indicates that the polysilazane-derived materials have the highest degree of homogeneity of micropores. The polysilazane-derived materials contain significant amount of micropores, e.g. HTT600NH possesses the highest amount of ultramicropores, and HTT600NHAr has the most homogeneous pore size distribution. On the other hand, the D-A analysis of the polysiloxane-derived samples indicate a higher degree of heterogeneity of pores compared to that of polysilazane-derived samples. The specimens which are subjected to ammonolysis step only (i.e. in HTT600NH and SPR600NH) possess polar surfaces.

The polycarbosilane-derived materials under similar processing conditions remain non-porous, indicated by the gas adsorption experiments. However, the SAXS experiments reveal that, these materials possess open micropores which are smaller than the size of probe molecules (CO₂ and N₂) used in the gas adsorption techniques. Such micropores with pore size < 0.35 nm could play a detrimental role in the hydrogen separation membranes where an effective pore size of around 0.3 nm is required.

Further structural studies are required to elucidate the role of nitrogen, incorporated into the SiCNO ceramics by the NH₃-assisted thermolysis as well as the mechanism of the microporosity development during the polymer-to-ceramic transformation.

Acknowledgements

The research leading to these results has received funding from the European Union Seventh Framework Programme (FP7/2007-2013) under grant agreement no 264873 (FUNEA – Functional Nitrides for Energy Applications). We authors would like to thank Hamburger Synchrotronstrahlungslabor (HASYLAB) at the Deutsches Elektronen - Synchrotron (DESY) Research Centre of the Helmholtz Association, in Hamburg, Germany for SAXS measurements (Proposal Nr. I-20110483, Insight into porosity of nanoporous metal doped polymer-derived-ceramics for energy and environmental applications). The authors would like to acknowledge Duan Li and Professor James Shen for the CO₂ adsorption measurements.

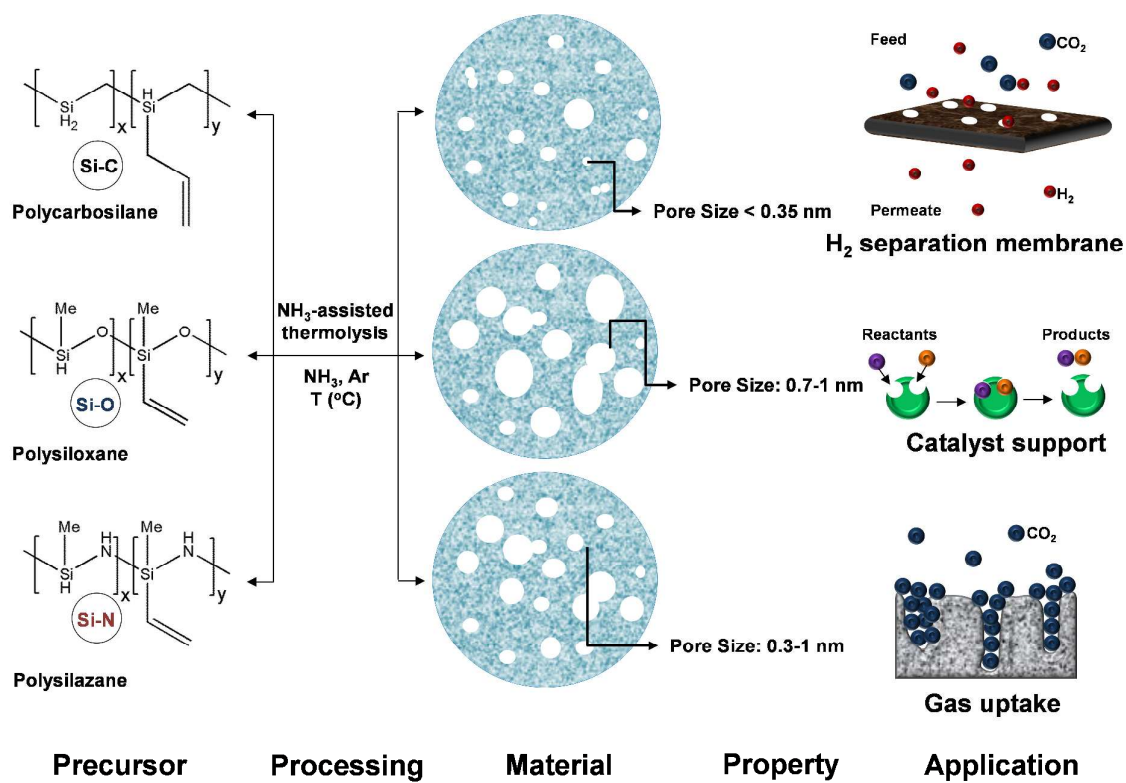
Electronic Supplementary Information (ESI) available: *Figure S1*: The tangent method illustrated for HTT600NHAr. *Figure S2*: N₂ adsorption isotherms for SMP600NH, SMP600NHAr, and SMPAr (a) and CO₂ adsorption isotherm for SMP600NHAr (b). *Figure S3*: FTIR spectra of HTT600NH and SPR600NH samples. *Figure S4*: SAXS curves of specimens derived from polycarbosilane, polysiloxane, and polysilazane precursors. *Figure S5*: Different SAXS profiles: a) Type 1, b) Type 2, and c) Type 3.

Notes and references

1. M. Seifollahi Bazarjani, M. Hojamberdiev, K. Morita, G. Q. Zhu, G. Cherkashinin, C. Fasel, T. Herrmann, H. Breitzke, A. Gurlo and R. Riedel, *J. Am. Chem. Soc.*, 2013, **135**, 4467-4475.
2. M. Seifollahi Bazarjani, M. M. Müller, H.-J. Kleebe, C. Fasel, R. Riedel and A. Gurlo, *J. Mater. Chem. A*, 2014, **2**, 10454-10564.
3. M. Seifollahi Bazarjani, H.-J. Kleebe, M. M. Müller, C. Fasel, M. Baghaie Yazdi, A. Gurlo and R. Riedel, *Chem. Mater.*, 2011, **23**, 4112-4123.
4. M. Seifollahi Bazarjani, M. M. Müller, H.-J. Kleebe, Y. Jüttke, I. Voigt, M. Baghaie Yazdi, L. Alff, R. Riedel and A. Gurlo, *ACS Appl. Mater. Interfaces*, 2014, 10.1021/am501892z.
5. Y. Juttke, H. Richter, I. Voigt, R. M. Prasad, M. Seifollahi Bazarjani, A. Gurlo and R. Riedel, *Chem. Eng. Trans.*, 2013, **244**, 1891-1896.
6. M. Hojamberdiev, R. M. Prasad, K. Morita, M. A. Schiavon and R. Riedel, *Micropor. Mesopor. Mat.*, 2012, **151**, 330-338.
7. R. M. Prasad, A. Gurlo, R. Riedel, M. Hubner, N. Barsan and U. Weimar, *Sensor Actuat. B-Chem.*, 2010, **149**, 105-109.
8. R. M. Prasad, Y. Iwamoto, R. Riedel and A. Gurlo, *Adv. Eng. Mater.*, 2010, **12**, 522-528.
9. B. Elyassi, W. X. Deng, M. Sahimi and T. T. Tsotsis, *Ind. Eng. Chem. Res.*, 2013, **52**, 10269-10275.
10. B. Elyassi, T. W. Kim, M. Sahimi and T. T. Tsotsis, *Mater. Chem. Phys.*, 2009, **118**, 259-263.
11. B. Elyassi, M. Sahimi and T. T. Tsotsis, *J. Membr. Sci.*, 2008, **316**, 73-79.
12. P. Colombo, G. Mera, R. Riedel and G. D. Soraru, *J. Am. Ceram. Soc.*, 2010, **93**, 1805-1837.
13. E. Ionescu, H. J. Kleebe and R. Riedel, *Chem. Soc. Rev.*, 2012, **41**, 5032-5052.
14. R. Riedel, G. Mera, R. Hauser and A. Klönczynski, *J. Ceram. Soc. Jpn.*, 2006, **114**, 425-444.

15. P. Colombo, D. C. Dunand and V. Kumar, *J. Mater. Res.*, 2013, **28**, 2187-2190.
16. P. Colombo and H. P. Degischer, *Adv. Eng. Mater.*, 2012, **14**, 1051-1051.
17. P. Colombo and H. P. Degischer, *Mater. Sci. Tech.*, 2010, **26**, 1145-1158.
18. Y. Iwamoto, *J. Ceram. Soc. Jpn.*, 2007, **115**, 947-954.
19. R. Hauser, S. Nahar-Borchard, R. Riedel, Y. H. Ikuhara and Y. Iwamoto, *J. Ceram. Soc. Jpn.*, 2006, **114**, 524-528.
20. S. Kaskel, K. Schlichte and B. Zibrowius, *Phys. Chem. Chem. Phys.*, 2002, **4**, 1675-1681.
21. E. Kockrick, P. Krawiec, U. Petasch, H. P. Martin, M. Herrmann and S. Kaskel, *Chem. Mater.*, 2008, **20**, 77-83.
22. W. Li and D. Zhao, *Chem. Commun.*, 2013, **49**, 943-946.
23. Y. F. Shi, Y. Wan and D. Y. Zhao, *Chem. Soc. Rev.*, 2011, **40**, 3854-3878.
24. J. Wan, M. J. Gasch and A. K. Mukherjee, *J. Am. Ceram. Soc.*, 2001, **84**, 2165-2169.
25. M. Hojamberdiev, R. M. Prasad, K. Morita, Y. F. Zhu, M. A. Schiavon, A. Gurlo and R. Riedel, *Appl. Catal. B-Environ.*, 2012, **115**, 303-313.
26. M. Hojamberdiev, R. M. Prasad, K. Morita, M. A. Schiavon and R. Riedel, *Micropor. Mesopor. Mat.*, 2012, **151**, 330-338.
27. M. Adam, M. Wilhelm and G. Grathwohl, *Micropor. Mesopor. Mat.*, 2012, **151**, 195-200.
28. P. Sonstrom, M. Adam, X. Wang, M. Wilhelm, G. Grathwohl and M. Baumer, *J. Phys. Chem. C*, 2010, **114**, 14224-14232.
29. M. Wilhelm, M. Adam, M. Baumer and G. Grathwohl, *Adv. Eng. Mater.*, 2008, **10**, 241-245.
30. M. Wilhelm, C. Soltmann, D. Koch and G. Grathwohl, *J. Eur. Ceram. Soc.*, 2005, **25**, 271-276.
31. H. Schmidt, D. Koch, G. Grathwohl and P. Colombo, *J. Am. Ceram. Soc.*, 2001, **84**, 2252-2255.
32. J. S. Bradley, O. Vollmer, R. Rovai, U. Specht and F. Lefebvre, *Adv. Mater.*, 1998, **10**, 938-942.
33. J. P. Dismukes, J. W. Johnson, J. S. Bradley and J. M. Millar, *Chem. Mater.*, 1997, **9**, 699-706.
34. O. Vollmer, F. Lefebvre and J. S. Bradley, *J. Mol. Catal. a-Chem.*, 1999, **146**, 87-96.
35. H. Schmidt, D. Koch, G. Grathwohl and P. Colombo, *J. Am. Ceram. Soc.*, 2001, **84**, 2252-2255.
36. J. P. Dismukes, J. W. Johnson, J. S. Bradley and J. M. Millar, *Chem. Mater.*, 1997, **9**, 699-706.
37. K. S. W. Sing, D. H. Everett, R. A. W. Haul, L. Moscou, R. A. Pierotti, J. Rouquerol and T. Siemieniowska, *Pure Appl. Chem.*, 1985, **57**, 603-619.
38. J. H. de Boer, B. G. Linsen, T. van der Plas and G. J. Zondervan, *J. Catal.*, 1965, **4**, 649-653.
39. K. Kaneko, *J. Membr. Sci.*, 1994, **96**, 59-89.
40. D. Burevski, *Colloid Polym. Sci.*, 1982, **260**, 623-627.
41. R. Ghosal and D. Smith, *J. Porous Mater.*, 1996, **3**, 247-255.
42. W. Rudzinski and D. H. Everett, *Adsorption of gases on heterogeneous surfaces*, Academic Press, London; San Diego, 1992.
43. D. Cazorla-Amorós, J. Alcañiz-Monge and A. Linares-Solano, *Langmuir*, 1996, **12**, 2820-2824.
44. F. Stoeckli and L. Ballerini, *Fuel*, 1991, **70**, 557-559.
45. M. M. Dubinin, *Carbon*, 1985, **23**, 373-380.
46. A. Guinier and G. Fournet, *Small-angle scattering of X-rays*, Wiley; Chapman and Hall, New York; London, 1955.
47. G. Laudisio, R. K. Dash, J. P. Singer, G. Yushin, Y. Gogotsi and J. E. Fischer, *Langmuir*, 2006, **22**, 8945-8950.
48. A. I. Kitaigorodskii, *X-Ray Structural Analysis of Fine-Grained and Amorphous Bodies* GITTL, Moscow, 1952.
49. R. N. Kyutt, E. A. Smorgonskaya, A. M. Danishevskii, S. K. Gordeev and A. V. Grechinskaya, *Phys. Solid State*, 1999, **41**, 1359-1363.
50. B. Y. Venhryn, I. I. Grygorchak, Y. O. Kulyk, S. I. Mudry and R. Y. Shvets, *Optica Applicata*, 2008, **38**, 119-125.
51. Y. Gogotsi, A. Nikitin, H. H. Ye, W. Zhou, J. E. Fischer, B. Yi, H. C. Foley and M. W. Barsoum, *Nature Mater.*, 2003, **2**, 591-594.
52. H. Schmidt, D. Koch and G. Grathwohl, *Chem. Eng. Technol.*, 2000, **23**, 959-964.
53. G. D. Soraru, Q. Liu, L. V. Interrante and T. Apple, *Chem. Mater.*, 1998, **10**, 4047-4054.
54. H. M. Williams, E. A. Dawson, P. A. Barnes, B. Rand, R. M. D. Brydson and A. R. Brough, *J. Mater. Chem.*, 2002, **12**, 3754-3760.
55. K. S. W. Sing and R. T. Williams, *Part. Part. Syst. Charact.*, 2004, **21**, 71-79.
56. D. Cazorla-Amorós, J. Alcañiz-Monge, M. A. de la Casa-Lillo and A. Linares-Solano, *Langmuir*, 1998, **14**, 4589-4596.
57. P. I. Ravikovitch, A. Vishnyakov, R. Russo and A. V. Neimark, *Langmuir*, 2000, **16**, 2311-2320.
58. A. Jánosi and H. F. Stoeckli, *Carbon*, 1979, **17**, 465-469.
59. J. F. Janik, W. C. Ackerman, R. T. Paine, D. W. Hua, A. Maskara and D. M. Smith, *Langmuir*, 1994, **10**, 514-518.
60. N. D. Hutson and R. T. Yang, *Adsorpt.-J. Int. Adsorpt. Soc.*, 1997, **3**, 189-195.
61. M. Thommes, *Chem. Ing. Tech.*, 2010, **82**, 1059-1073.
62. H. W. Yang, A. M. Khan, Y. Z. Yuan and S. C. Tsang, *Chem. Asian J.*, 2012, **7**, 498-502.
63. A. Gibaud, J. S. Xue and J. R. Dahn, *Carbon*, 1996, **34**, 499-503.
64. M. Kalliat, C. Y. Kwak and P. W. Schmidt, in *New Approaches in Coal Chemistry*, American Chemical Society, Washington DC, 1981, pp. 3-22.
65. P. B. Hirsch, *Math. Phys. Sci.*, 1954, **226**, 143-169.
66. S. T. Oyama, D. Lee, P. Hacarlioglu and R. F. Saraf, *J. Membr. Sci.*, 2004, **244**, 45-53.
67. V. Boffa, H. L. Castricum, R. Garcia, R. Schmuhl, A. V. Petukhov, D. H. A. Blank and J. E. ten Elshof, *Chem. Mater.*, 2009, **21**, 1822-1828.
68. V. Boffa, J. E. ten Elshof, A. V. Petukhov and D. H. A. Blank, *Chemosuschem*, 2008, **1**, 437-443.
69. S. Naserifar, W. A. Goddard, L. C. Liu, T. T. Tsotsis and M. Sahimi, *J. Phys. Chem. C*, 2013, **117**, 3320-3329.
70. Q. Liu, W. Shi, F. Babonneau and L. V. Interrante, *Chem. Mater.*, 1997, **9**, 2434-2441.
71. D. Farrusseng, K. Schlichte, B. Spliethoff, A. Wingen, S. Kaskel, J. S. Bradley and F. Schuth, *Angew. Chem. Int. Edit.*, 2001, **40**, 4204-4207.

72. J. S. Bradley, O. Vollmer, R. Rovai, U. Specht and F. Lefebvre, *Adv Mater*, 1998, **10**, 938-942.
73. O. Vollmer, F. Lefebvre and J. S. Bradley, *J Mol Catal a-Chem*, 1999, **146**, 87-96.
74. S. Kaskel, K. Schlichte and B. Zibrowius, *Phys Chem Chem Phys*, 2002, **4**, 1675-1681.
75. S. Kaskel and K. Schlichte, *J Catal*, 2001, **201**, 270-274.
76. S. Kaskel, D. Farrusseng and K. Schlichte, *Chem Commun*, 2000, 2481-2482.
77. S. Hassan, A. L. Hector, J. R. Hyde, A. Kalaji and D. C. Smith, *Chem Commun*, 2008, 5304-5306.
78. P. Hacırlıoğlu, D. Lee, G. V. Gibbs and S. T. Oyama, *J Membrane Sci*, 2008, **313**, 277-283.
79. S. T. Oyama, D. Lee, P. Hacırlıoğlu and R. F. Saraf, *J Membrane Sci*, 2004, **244**, 45-53.



The NH_3 -assisted synthesis strategy from preceramic polymers provides tools to engineer the porosity of microporous SiCNO ceramics for potential applications in the fields of catalysis, gas adsorption and gas separation.